

Modeling Synthetic Jets for Low-Re Airfoil Unsteady Flow Control

Vladimir V. Golubev and Hany K. Nakhla

Florida Center for Advanced Aero-Propulsion, Embry-Riddle Aeronautical University
Daytona Beach, FL 32114, USA, Vladimir.Golubev@erau.edu
Department of Applied Engineering Technology, North Carolina A&T State University,
Greensboro, NC 27411, USA, hknakhla@ncat.edu

ABSTRACT

Synthetic jet actuators (SJAs) may be carefully designed to alleviate the negative impact of impinging flow non-uniformities on the aircraft wing unsteady aerodynamic response. The current study investigates the effectiveness of SJAs for active control of unsteady flow over SD7003 low-Re airfoil in presence of a high-amplitude upstream flow disturbance characterized by a sharp-edge gust. In the adopted numerical procedure, the actuator's dimensional scaling and excitation frequency effects are first examined for a specific SJA configuration using a Lumped Element Model. The next step employs a Reynolds-averaged Navier-Stokes analysis to determine simple fluctuating-velocity boundary condition at the bottom of the actuator's orifice. The orifice with the properly defined boundary condition is then embedded into the airfoil surface for conducting high-accuracy viscous analysis of active flow control during gust-airfoil interaction process. Results of numerical simulations indicate that the SJA positive effect on the airfoil response appears most significant with the actuator operating in resonance with the airfoil natural shedding frequency.

1. INTRODUCTION

The current work is part of an ongoing multidisciplinary study aimed at developing an integrated flow/flight/propulsion control system for a fixed-wing micro air vehicle (MAV) operating in a gusty urban environment. The proposed control system would use a carefully distributed array of zero-net-mass-flux (ZNMF) synthetic-jet actuators (SJAs) with optimized performance characteristics. Various performance characteristics of a single actuator (illustrated in Figure 1) such as the jet formation criteria and micro-thrust production were previously addressed in Refs. [1–3] using nonlinear inviscid and viscous models for resonator cavities as well as unsteady Reynolds-averaged Navier-Stokes (RANS) simulations of synthetic jet flowfields. The obtained RANS solutions were validated against experimental and Implicit Large Eddy Simulation (ILES) data for Reynolds numbers (based on the jet nozzle diameter/width d) in the range of $Re_d = 500$ – 1000 , both for the axisymmetric and planar jet configurations in the laminar and turbulent flow regimes. An adequate comparison against experimental and previously validated high-fidelity numerical predictions was achieved using RANS analysis with Reynolds-Stress turbulence model employed in conjunction with the dynamic grid adaption [3]. This approach is also used in the present study and is coupled with a Lumped Element Model (LEM) procedure of Gallas et al. [4] to examine scaling of the actuator performance. The study then focuses on the issues of MAV active flow control using a planar synthetic jet actuator used in Ref. [3] as the baseline case and previously investigated experimentally by Smith and Glezer [5] and numerically by Rizzetta et al. [6].

The aerodynamic performance of a small-size (less than 15–20 cm in wing span) low-Re MAV flyers has been the subject of numerous studies, as reviewed, e.g., by Mueller and DeLaurier [7], Gad-el-Hak [8], and Shyy et al. [9]. In general, in the typical MAV range of the airfoil chord-based Reynolds number $Re_c = 10^4$ – 10^6 , the airfoil boundary layer remains laminar at the onset but the performance is dictated by the flow poor resistance to separation. The resulting free-shear layer is highly unstable and the flow may quickly transition to turbulent regime. The separated region may further reattach due to increased entrainment and form the separation bubble [9]. The exact formation and subsequent breakdown processes are highly sensitive to Reynolds number, Re_c , and to a large degree affect the airfoil lift-to-drag ratio with strong lift hysteresis vs. angle-of-attack. More specifically, for a delta-wing configuration currently considered for the fixed-wing MAV model, the steady-state flow is characterized by a pair of counter-rotating leading-edge vortices (LEVs) sensitive to breakdown at higher angles of attack. Causing low pressure over the wing, LEVs may contribute up to 40% of the

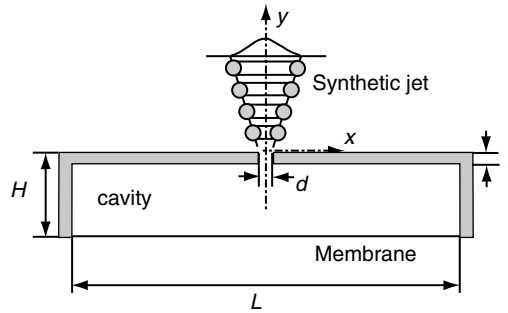


Figure 1. Schematic of synthetic-jet actuator.

total lift. As presented by Gursul et al. [10], the flow re-attachment is a crucial element of the lift-enhancement flow control strategy, and, in fact, is achievable for non-slender geometries, even after the vortex breakdown reaches the wing apex. In particular, while the unsteady excitation has little effect on the vortex breakdown, it can excite the Kelvin-Helmholtz instability of the separated shear layer, and thereby promote re-attachment. The latter phenomenon was successfully demonstrated by Williams et al. [11] using active flow control through pulsed blowing at the leading edge.

The effects of gusty urban environment and wing aeroelasticity on MAV performance have been extensively studied in the context of airfoil-gust and airfoil-vortex interactions by Golubev et al. [12–16]. High-fidelity analyses of nonlinear viscous interactions of time-harmonic gust configurations with stationary and plunging/pitching airfoil were first conducted in Ref [12] and later extended to examine the gust response of the two-degrees-of-freedom (2-DOF) elastically-mounted MAV wings [13]. In the implemented iterative procedure, the governing Navier-Stokes equations were solved simultaneously with equations of motion of the structure, so that the fluid and structure were treated as a coupled dynamic system. Flexible airfoil response to a high-amplitude time-harmonic gust was examined elucidating details of the wing section nonlinear transition to limit-cycle oscillations. Such prediction capability is essential for future detailed studies of SJA-based active flow control (AFC) strategies for mitigating unsteady response of a realistic MAV wing in a gusty urban environment.

The current study for the first time numerically investigates SJA effectiveness for control of unsteady flow over low-Re airfoil in the presence of a high-amplitude upstream flow disturbance. The unsteady responses of SD7003 fixed-wing airfoil to canonical configurations of the impinging vortical gusts have been recently examined in parametric studies [14–16] conducted in the laminar flow regime with $M_\infty = 0.1$ and $Re_c = 10,000$. The canonical gust models included the time-harmonic gust and the sharp-edge gust with variable frequency, duration and amplitude, and the Taylor vortex with variable size, strength, sense of rotation and initial position relative to the airfoil leading edge. Figure 2a

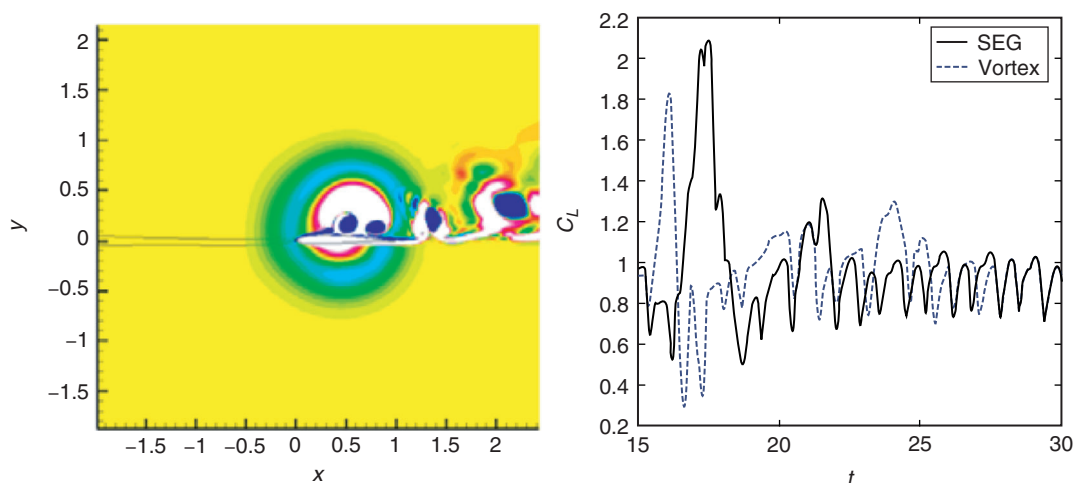


Figure 2. (a) Vorticity contours for vortex impinging on the airfoil, (b) Lift responses to the impinging vortex and sharp-edge gust; from Ref. [15].

illustrates the vorticity contours for the Taylor vortex with positive (counterclockwise) sense of rotation passing through the airfoil in a head-on collision. The vortex generates the maximum upwash of 35% of the mean flow induced on the airfoil installed at the angle of attack $\alpha = 8^\circ$. Figure 2b shows the comparison of the airfoil resulting high-amplitude unsteady lift responses to the vortex and the sharp-edge gust with equivalent induced angle of attack and duration. Note that the effect of the impinging disturbance may be even more devastating for longer gust duration (or larger vortex core) as the airfoil transitions into stall and exhibits a prolonged recovery period following the passage of the disturbance. Such studies imply a need to investigate effective means of unsteady flow control using novel AFC approaches.

As recently reviewed by Rumsey [17], the analysis of SJA-based AFC control of separated airfoil flows using complete surface-embedded actuator configuration including a resonator and a moving diaphragm can in principle be realized without any simplifying assumptions with a high-accuracy numerical approach. In this regard, LES has been the most successful technique but computationally very expensive [18]. On the other hand, RANS methods have had a limited success in application to separated flows in general.

To examine SJA effectiveness for control of separated flow in low-Re gust-airfoil interactions, a numerical procedure is developed involving several steps. In the first step, the actuator excitation parameters and geometry are examined for scaled designs using LEM model to match the required synthetic jet characteristics. Next, the results of RANS simulations for SJA in quiescent medium are obtained for specified actuator geometry to examine profile of the jet velocity at the actuator orifice's exit and bottom. Finally, high-accuracy viscous simulations of separated airfoil flows are conducted with the actuator orifice embedded in the airfoil surface at a selected location. In general, the pre-determined, RANS-generated velocity at the orifice bottom can be specified as the orifice boundary condition. Instead, the current test study implements a computationally more efficient approach suggested by Raju et al. [19] wherein the boundary conditions are imposed at the bottom of the orifice in the form of simple time-harmonic oscillations with matched amplitude without modeling the complete cavity flow.

In the following sections, details of LEM/RANS scaling analyses employed to specify the boundary condition for the actuator are discussed first. Next, test examples of high-accuracy viscous simulations for sharp-edge gust-airfoil interactions are conducted with AFC on and off to examine synthetic-jet flow fields generated in the actuator's orifice and the effect of jet interaction with separated low-Re grazing flow on the airfoil unsteady aerodynamic response.

2. LEM AND RANS SJA MODELING

In the current approach, parameters of SJA design at different scales are first evaluated using LEM model by Gallas et al [4]. Such model is based on the assumption that the characteristic length scales of the governing physical phenomena are much larger than the largest geometric dimension. In this case valid for relatively low excitation frequencies, the governing partial differential equations for the distributed system may be "lumped" into a set of coupled ordinary differential equations and the system can be represented by an equivalent electrical circuit with typical discrete elements [4].

The LEM model thus represents a low-fidelity analysis tool that can be very effectively used to estimate the bulk dynamic response of the synthetic jet for a preliminary design of SJA-based flow control system. Note that such response results from a nonlinear coupling between the cavity and the diaphragm resonant properties. Particularly, in the example considered in the current work for a planar SJA with the orifice slot span of 15 mm [5], the LEM-based SJA scaling process incorporates the following steps: (i) Adopting the baseline case (previously validated in numerical simulations) from Ref. [6] for the actuator's orifice width and height $d = l = 0.5$ mm and the cavity width and height $L = 15d$ and $H' = H - l = 10d$, respectively (Figure 1); (ii) Determining the physical properties of the piezoelectric transducer and excitation voltage that match the results of the baseline case; (iii) Scaling the SJA geometrical parameters to examine optimal designs appropriate for AFC control of the selected airfoil. The dynamic responses of the scaled SJA designs in Figure 3 show two coupled resonant frequencies related to the properties of the SJA piezoelectric membrane as well as actuator cavity and orifice dimensions. For the fixed diaphragm properties, the first mode is stationary and close to 800 Hz while the second mode varies with the actuator scaling ratio. For instance, the results from LEM-based scaling analysis indicate that SJA with $d = 0.125$ mm would deliver the second peak of the average jet velocity when the actuator is excited at the resonance frequency $f \sim 4$ kHz. Such scaling study thus helps to identify the SJA design parameters in terms of the frequency response and the average synthetic-jet velocity produced for each selected actuator size, for the given diaphragm properties.

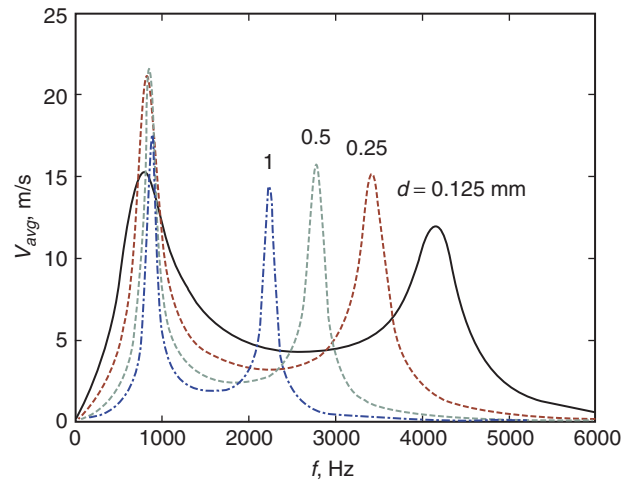


Figure 3. Frequency response of scaled SJA models based on LEM [4] modeling.

Once the preliminary LEM-based SJA designs are developed, the next stage should involve high-fidelity viscous simulations to account for the nonlinear effects related to the actuator flow vorticity dynamics and to obtain the flow statistics necessary for the final stage of the AFC control study. The current study employs the RANS approach previously implemented in Ref. [3] to conduct the analysis of selected actuator designs. The transient analysis using ANSYS-CFX software is carried out using the second-order finite-volume discretization scheme used in conjunction with the second-order implicit time marching. The analysis is first validated for the baseline case of Ref. [6], with the assumed uniform membrane displacement governed by

$$y_d = -H + y_{dm} \sin(2\pi f_a t) \quad (1)$$

for $y_{dm}/d = 0.41$ and the actuation frequency $f_a = 1$ kHz. The dynamically-adapted mesh details near the orifice and the computed vorticity contours are shown, respectively, in Figures 4a and 4b revealing the high-gradient mesh regions as well as the periodic generation and further convection of the vortical structures forming the synthetic jet (half-planes of the cavity, orifice and external flow domains are shown above the jet axis). The time variation of the jet centerline velocity (non-dimensionalized by $V_{ref} = 22$ m/s) at the distance $y/d = 5$ above the SJA orifice (Figure 1) is shown over the period of jet excitation $T = 1/f_a$ in Figure 5. Comparison of RANS simulations using two turbulence models against the ILES predictions of Ref. [6] reveals the best match obtained with BSL Reynolds Stress (RS) turbulence model thus employed in all further computations.

Based on LEM scaling analysis, the SJA design selected for AFC control of unsteady airfoil flows has the orifice of width $d = 1$ mm. Relative to the benchmark case with $f_a = 1$ kHz, the SJA model with the scaled membrane produces the maximum jet exit velocity amplitude at the diaphragm actuation frequency of $f_a = 500$ Hz. Note that the displacement volume for oscillating cavity flow thus remains unchanged.

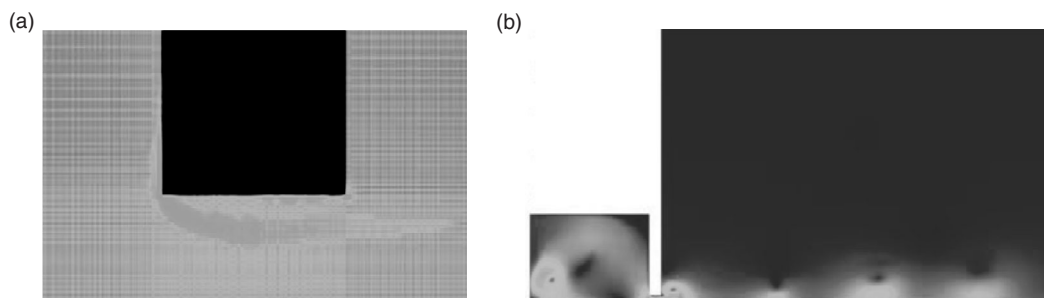


Figure 4. Results of SJA RANS simulations for benchmark case of Ref. [6]: (a) Details of near-orifice dynamically-adapted mesh, (b) Computational domain with vorticity contours.

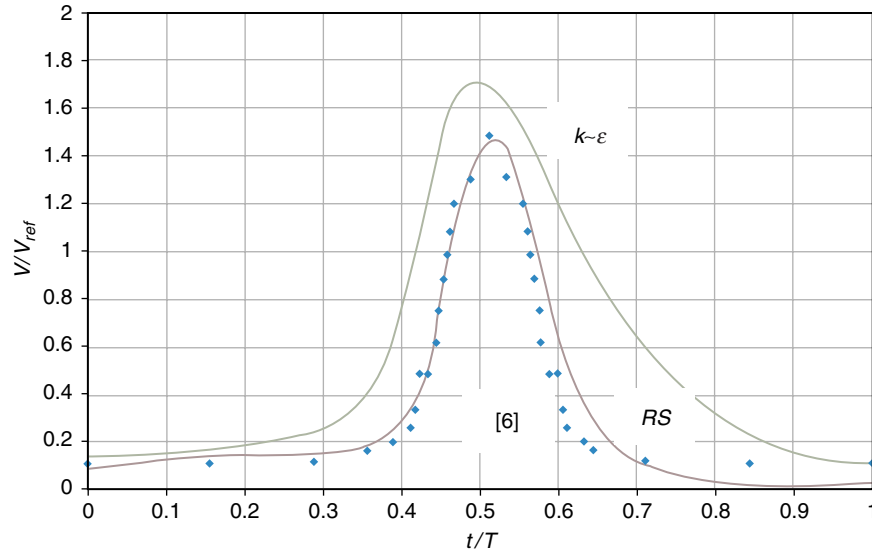


Figure 5. Comparison of synthetic jet centerline velocity variation at $y/d = 5$ over the period of SJA excitation.

The corresponding results for the peak and average velocity at the inlet and exit of the orifice are shown in Figure 6. In addition, the results for the scaled SJA design with $f_a = 300$ Hz are included to be employed in the subsequent AFC study. In the latter case, the SJA suboptimal operation characterized by the reduced displacement volume and higher recirculating flow at the orifice produces lower jet velocity amplitude. While further optimization of the SJA design would improve the performance, the test example of AFC control employs such operating condition to match with the airfoil unsteady flow characteristics in the

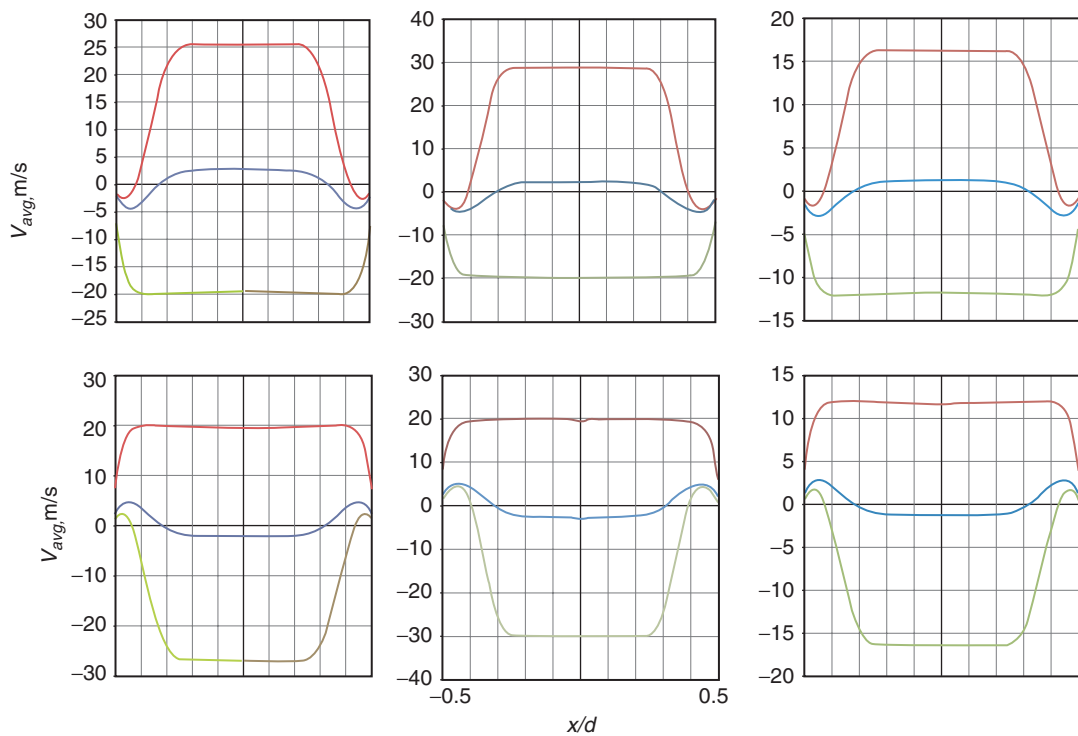


Figure 6. Peak (in/out) and average jet velocity profiles at SJA orifice exit (upper plots) and bottom (lower plots) obtained for (left to right) $d = 0.5$ mm and $f_a = 1$ kHz, $d = 1$ mm and $f_a = 500$ Hz, $d = 1$ mm and $f_a = 300$ Hz.

manner discussed further below. Finally, it is important to note that the distribution of the jet outflow velocity at the orifice bottom appears nearly uniform, which thus provides basis for assuming a simplified form of the boundary conditions for the SJA further adopted in the AFC control study.

3. AIRFOIL FLOW CONTROL MODELING

3.1. Numerical model

The effects of synthetic-jet actuation applied to low-Re unsteady flow over airfoil is analyzed using a high-accuracy viscous solver FDL3DI [20] used in the previous gust-airfoil and vortex-airfoil interaction studies [12–16]. The following features of the employed numerical procedure appear particularly beneficial for the current application:

- Implicit time marching algorithms (up to 4th-order accurate) are suitable for the low-Re wall-bounded flows.
- High-order spatial accuracy (up to 6th-order accurate) is achieved by use of implicit compact finite-difference schemes, thus making LES resolution attainable with minimum computational expense.
- Robustness is achieved through a low-pass Pade-type non-dispersive spatial filter that regularizes the solution in flow regions where the computational mesh is not sufficient to fully resolve the smallest scales. Note that the governing equations are represented in the original unfiltered form, used unchanged in laminar, transitional, or fully turbulent regions of the flow. The resulting Implicit LES (ILES) procedure employs the high-order filter operator in lieu of the standard SGS and heat flux terms. The resulting filter thus selectively damps the evolving poorly resolved high-frequency content of the solution.
- Overset grid technique is adopted for geometrically complex configurations, with the high-order interpolation maintaining spatial accuracy at overlapping mesh interfaces.

The approach was previously tested against various benchmarks [20] and was successfully involved in flow control predictions by Rizzetta et al [6] and Morgan et al [18]. The current version of the code employs the developed and successfully tested capability for the high-fidelity analysis of unsteady flow-structure interactions including accurate descriptions of upstream unsteady vortical flowfields used in the current study.

3.2. Numerical case study and implementation

The current test study performs two-dimensional numerical simulations of the stationary SD7003 airfoil in the laminar flow regime with $M_\infty = 0.1$ and $Re_c = 10,000$, with all variables non-dimensionalized by the airfoil chord c , and freestream flow density ρ_∞ and flow velocity u_∞ .

The background steady-state flow corresponds to the airfoil installed at the angle of attack $\alpha = 8^\circ$ thus nearing the stall condition. In the gust-airfoil interaction simulations, the steady-state flowfield is first obtained by marching in time for 15–20 characteristic cycles (based on the wake-shedding Strouhal number, $St_\alpha = f_s c \sin\alpha / u_\infty \sim 0.2$) to guarantee a time-asymptotic nearly-periodic state. The unsteady computations with upstream-generated upstream flow perturbation and synthetic-jet actuation then start at $t = 15$.

In the current simulations, the sharp-edge gust (SEG) perturbation (Figure 7) is produced upstream of the airfoil and described in terms of the upwash velocity profile induced on the airfoil surface,

$$v_g = \begin{cases} \varepsilon_g h(t - x / u_\infty), & u_\infty(t - T_g) \leq x \leq u_\infty t \\ 0, & \text{otherwise} \end{cases} \quad (2)$$

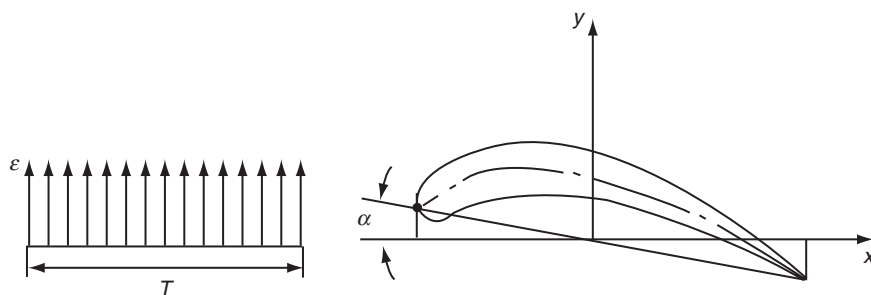


Figure 7. Sharp-edge gust-airfoil interaction model.

where ε_g and T_g are, respectively, the gust amplitude and duration. Note that although $h(t-x/u_\infty) = 1$ is imposed in the analysis, the gust forced through the solver momentum equations at an upstream source region (as described in Ref. [15]) gradually ramps up and then ramps down after the gust duration T_g due to fluid inertia, similar to natural flows.

A fixed time step with $\Delta t = 2 \times 10^{-4}$ is chosen for the implicit time marching. Results presented here are obtained from the code parallel simulations using ERAU's 262-processor Beowulf Zeus cluster (64-bit, 3.2 GHz Intel Xeon, 4GB RAM systems), with the mesh efficiently partitioned into 96 overlapped blocks assigned to different processors. Grid independence of numerical results was tested using the coarse $327 \times 198 \times 3$ and the fine $466 \times 395 \times 3$ original O-meshes generated about SD7003 airfoil. The results generally reveal very close aerodynamic responses obtained during the impact, with some deviations present in the recovery period. Based on the analyses in Refs [14–15], both meshes provide adequate spatial resolution for the selected Reynolds number. However, the latter grid employs a refined clustering on the suction side especially towards the trailing edge for more accurate resolution of the enhanced boundary-layer vorticity dynamics and its shedding into the wake. It is thus used as the baseline grid in the subsequent analysis, with the mesh details near the airfoil surface shown in Figure 8a.

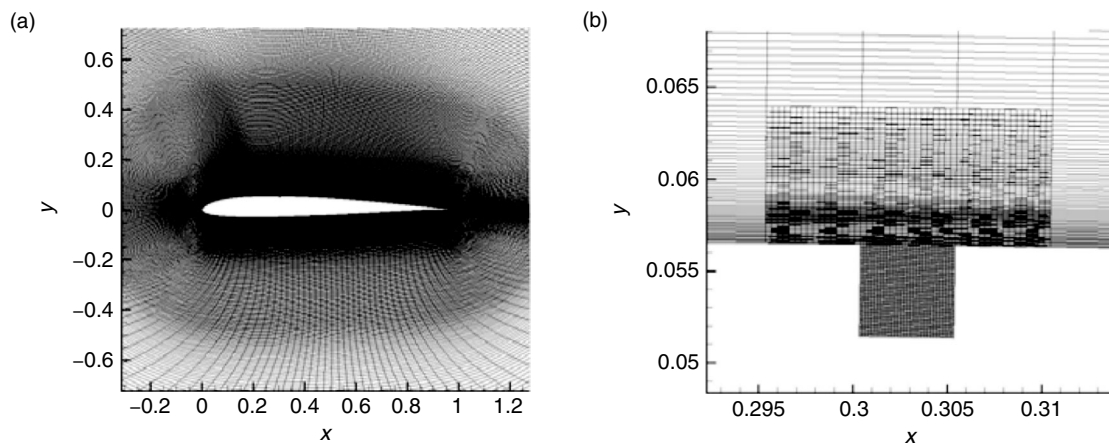


Figure 8. (a) Sectional 466×395 grid, (b) Details of overset meshes in SJA orifice region.

In computations, the freestream conditions are imposed at the farfield boundary located more than 100 chords away from the airfoil, with the grid rapidly stretching towards that boundary to ensure effective elimination of spurious reflections achieved in conjunction with the low-pass spatial filtering [20].

Modeling of the synthetic-jet actuator is realized through embedding the actuator's orifice mesh (previously employed in RANS simulations) in the airfoil surface and providing an adequate overlap with the original airfoil mesh (Figure 8b). The proper implementation of the employed overset grid methodology involves 6 meshes generated using Pointwise© software in the near-orifice overlap region. The overset grid connectivity is established using NASA's PEGASUS [21] and AFRL's BELLERO [22] software, with the connectivity data produced by the former serving as input for the latter handling grid decomposition and establishing the intra-grid communication required for the grid system subdivided into blocks for parallel processing. More details of the employed overset mesh procedures can be found in Ref. [22].

3.3. Selection of SJA parameters

In the current study, the receptivity of a separated laminar flow to the unsteady forcing is examined for the actuator's orifice embedded about $0.3c$ downstream from the leading edge on the airfoil suction side in the area where a laminar separation zone forms based on the steady-state simulations, as observed in Figure 9a. The ratio of the orifice width to the airfoil chord is fixed at $d/c = 0.005$.

To determine the optimal SJA performance and achieve required flow receptivity, several parameters are first considered. For compressible flows, Seifert and Pack [23] suggested that the optimal non-dimensional actuation frequency $F^+ = f_a x_{te}/u_\infty$ should be $O(1)$, where f_a is the actuation frequency in Hz and x_{te} is the distance from the actuator to the airfoil trailing edge. Another important parameter is

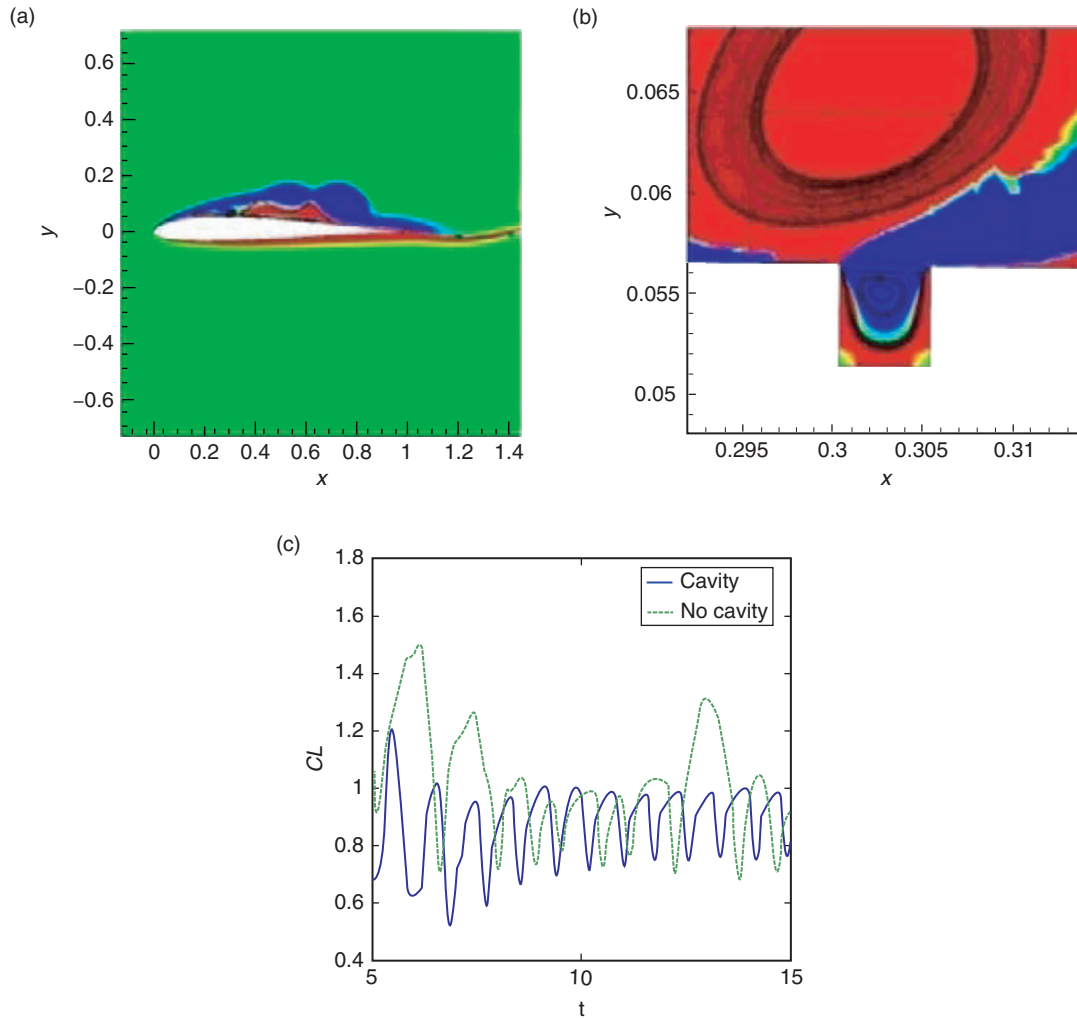


Figure 9. (a) Instantaneous vorticity contours and streamlines for steady-state flow condition without actuation, (b) Corresponding solution details in the actuator region, (c) Airfoil unsteady lift response with and without embedded SJA orifice cavity.

the jet momentum coefficient defined by McCormick [24] as the ratio $C_{\mu} = (\rho d V_j^2) / (\rho c u_{\infty}^2)$ where V_j is the peak jet velocity at the orifice exit. The latter should generally exceed the value of around 0.002 for any substantial effects on the flow to be observed [25]. Finally, general formation criteria for synthetic jets are given in Ref. [26] and have been previously evaluated in Ref. [3]. It should be clarified that the issue of the optimal SJA design for a required performance is unrelated in this context.

To illustrate how various parameters characterizing SJA performance are affected by the choice of dimensional flow and geometry characteristics, consider the case of $u_{\infty} = 30$ m/s and $c = 0.2$ m taken in the context of characteristic MAV dimensions and numerical parameters selected for SD7003 airfoil numerical simulations. In the test study of Section 2, RANS SJA simulations have been conducted with actuation frequency $f_a = 300$ Hz which corresponds to the non-dimensional angular frequency $\omega_a = 2\pi f_a c / u_{\infty} = 12.6$ fixed in the current airfoil simulations. This provides with $F^+ \approx 1.4$ for $x_{le} = 0.7c$. In addition, the case with $\omega_a = 9$ is also examined which matches the von Karman shedding frequency for the airfoil steady-state flow regime and corresponds to $F^+ \approx 1$. Furthermore, with the ratio $d/c = 0.005$ fixed in all computations, the criterion $C_{\mu} \geq 0.002$ considered here for incompressible flow indicates the minimum required peak jet velocity at the orifice exit, $V_j \approx 19$ m/s which is nearly matched in RANS SJA simulation for this case ($d = 1$ mm), with corresponding results for the jet velocity profiles shown in Figure 6. Note that the incompressible peak velocity values may significantly overpredict the actual results. On the other hand, for a comparable SJA geometry with $f_a = 100$ Hz considered by Tang and Zhong [27], the compressibility effects are shown to become dominant for $d \leq 0.75$ mm. Overall, it is

concluded that the current SJA configuration should have a noticeable effect on the airfoil boundary-layer dynamics.

It could be noted that for the considered example with $c = 0.2$ m, the actual $Re_c \sim 4.3 \times 10^5$ based on the characteristic free-stream air conditions in a typical urban environment indicates a fully turbulent boundary-layer regime. On the other hand, the current two-dimensional airfoil simulations assume a laminar mean flow with $Re_c = 10^4$. While the SJA effect on separated turbulent flow control will be addressed in future three-dimensional ILES studies, it is revealing to make dimensional estimates assuming, e.g., $c = 0.025$ m in which case the resulting $Re_c \sim 5.4 \times 10^4$ for SD7003 airfoil corresponds to the transitional boundary layer [28] with the flow physics close to the currently considered flow regime. Note that with $d = 0.125$ mm, the fixed $\omega_a = 12.6$ ($f_a = 2400$ Hz) and $\omega_a = 9$ ($f_a = 1700$ Hz) would not change the corresponding values of F^+ and the minimum required jet peak velocity at the orifice exit based on $C_\mu \geq 0.002$ (with compressibility now playing a major role). Also, the scaling analysis of Section 2 performed for $d = 0.125$ mm reveals the second peak value of 25 m/s for the scaled actuation frequency $f_a = 4000$ Hz ($\omega_a \approx 21$), with the latter dominated by the actuator's Helmholtz resonator properties. For the given SJA design characteristics, the jet exit velocity would be somewhat reduced for the actuation frequencies considered in the current airfoil simulations.

3.1.1. SJA Boundary Condition

With the SJA orifice mesh embedded in the airfoil surface, the adopted numerical procedure imposes the boundary conditions at the bottom of the orifice matched to the corresponding RANS solutions illustrated in the bottom plots of Figure 6. To simplify the numerical formulation, the current test study follows Ref. [19] which suggests imposing a simple time-harmonic velocity fluctuation thus achieving a good comparison with results obtained from the full actuator cavity simulations. Furthermore, a single velocity component normal to the orifice bottom is considered in the current work. As shown in Figure 6 for the scaled SJAs ejecting the fluid into the quiescent medium, the jet positive peak velocities at the exit of the orifice reach 15–30 m/s corresponding to the positive peak velocities of 12–20 m/s at the bottom of the orifice. In the current test simulations, a value of 15 m/s is assumed for the latter. Hence, with the solver non-dimensionalization, the following simple expression for the resulting fluctuating velocity at the bottom of the orifice is employed,

$$v_{SJA} = 0.5 \cos(\omega_a t) \quad (3)$$

In numerical simulations, the actuation of the cavity starts at $t = 15$, simultaneously with SEG generation in cases with the imposed upstream flow disturbance.

4. RESULTS

4.1. Results for steady-state flow condition (AFC off)

Results of steady-state flow simulations with $M_\infty = 0.1$ and $Re_c = 10,000$ in Figure 9a,b show the vorticity contours and streamlines and demonstrate how SJA orifice embedded in the airfoil surface (still with no actuation) generates a well-defined vortical structure inside the cavity. A much larger and stronger vortical structure is formed outside in the airfoil boundary layer. Very minor discontinuities in the vorticity contours are produced at the interface between the airfoil and SJA grids due to the local accuracy loss in the interpolation region but overall the solution appears very reasonable. It is interesting to note phase deviations and even some frequency shift in the established steady-state lift oscillations observed with and without embedded SJA orifice cavity in Figure 9c. Moreover, the apparent boundary-layer tripping effect produced by the cavity appears to regularize the shedding process without significant impact on the unsteady response mean values.

4.2. Airfoil response with AFC on ($\omega_a = 9$), no SEG

The time-periodic unsteady forcing of the airfoil boundary layer with the velocity profile (3) imposed at the bottom of the embedded actuator's orifice results in a modification of the boundary-layer vorticity and the corresponding aerodynamic responses. Figure 10 illustrates the resulting dynamics of the unsteady flow around the airfoil by showing the vorticity contours and streamlines at four moments of time (left to right) $t = 19.8, 20.04, 20.26$ and 20.5 , over a single period of actuation $T_a \approx 0.7$ corresponding to $\omega_a = 9$. The respective bottom plots in Figure 10 focus on the near-orifice area revealing the fluctuating jet velocity during the flow injection and expulsion phases. Note how the jet

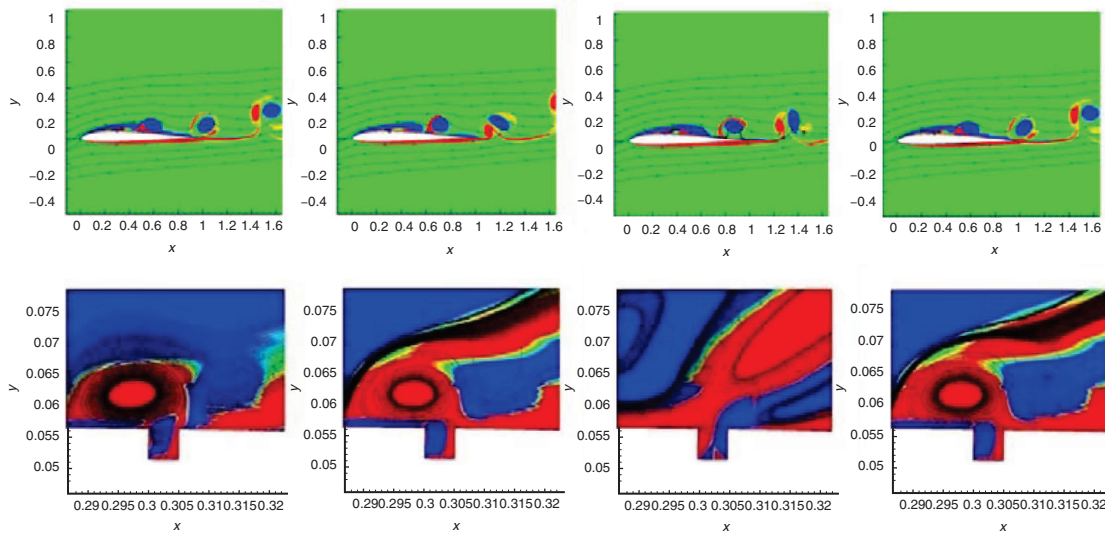


Figure 10. Instantaneous vorticity contours and streamlines over the actuation period, $\omega_a = 9$.

interaction with the grazing flow completely modifies the axisymmetric jet structure in comparison with the case of SJA performance in a quiescent medium. The time histories of the unsteady aerodynamic lift, drag and quarter-chord moment airfoil responses in Figure 11 indicate noticeable effects of the actuation. Those appear more pronounced for drag and moment responses where the shifts in the mean values are clearly observed.

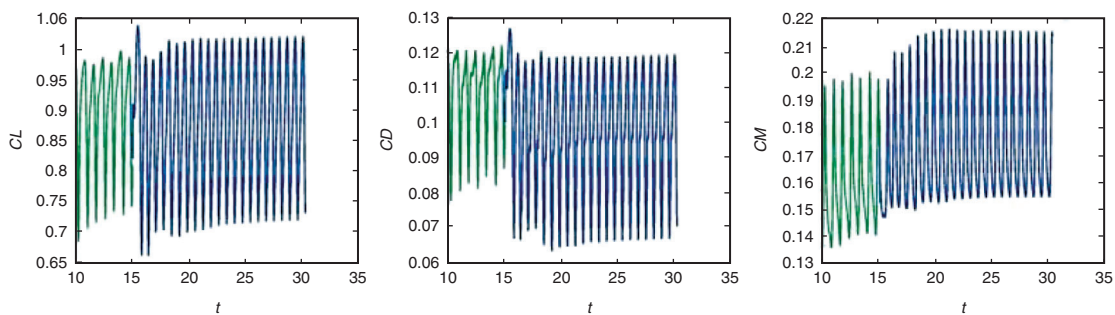


Figure 11. Airfoil aerodynamic response with AFC on, $\omega_a = 9$.

4.3. Airfoil response to SEG with AFC on ($\omega_a = 12.6$)

With the sharp-edge gust, imposed with amplitude $\varepsilon_g = 0.35$ and duration $T_g = 5$ in Eq. (2), impinging on the airfoil surface, the pattern of the boundary-layer vorticity dynamics dramatically changes, as illustrated in the top plots of Figure 12 with AFC off. The process of the airfoil abruptly entering into the stall can be clearly observed, with Refs [14–15] providing full details of the parametric study conducted for this gust-airfoil interaction problem.

The bottom plots in Figure 12 show the corresponding results obtained with AFC on which reveal significant actuation effect on the gust-stalled flow dynamics. All results are shown at four moments of time (left to right) $t = 20.9, 21.06, 21.22$ and 21.40 , over the actuation period $T_a \approx 0.5$ corresponding to $\omega_a = 12.6$. The near-orifice plots in Figure 13 show details of SJA performance and resulting modification in the boundary-layer vorticity dynamics. Overall, the differences are apparent and reveal noticeable SJA effect on the stalled flow dynamics.

The comparison of time histories of aerodynamic responses in Figure 14 further details the SJA impact on separated flow dynamics. As expected, the effects of boundary-layer receptivity are more pronounced in the drag response. On the other hand, the peak response values with AFC on appear

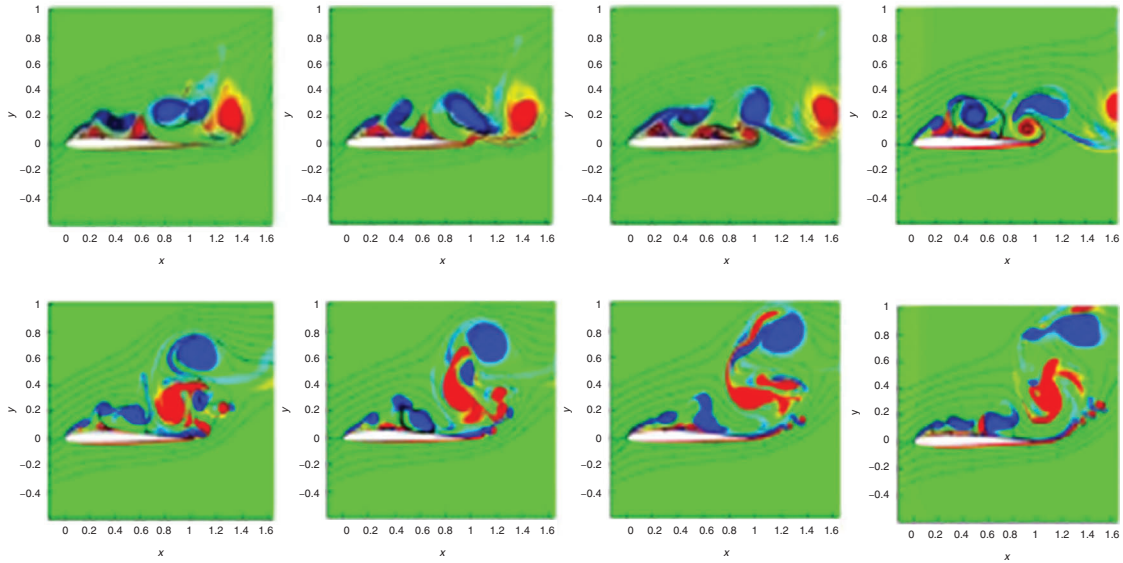


Figure 12. Instantaneous vorticity contours and streamlines over the actuation period with AFC off (top plots) and on (bottom plots) for gust-stalled airfoil, $\omega_a = 12.6$.

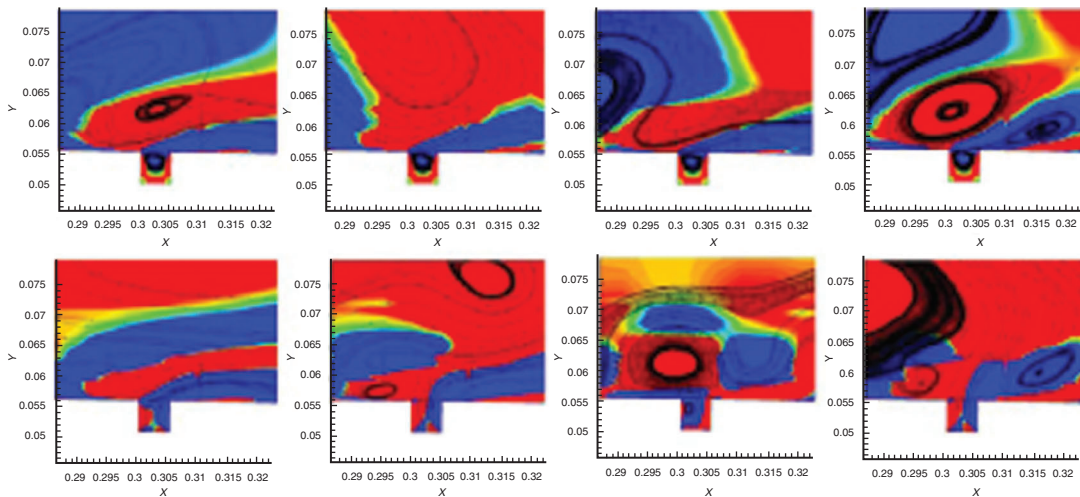


Figure 13. Near-SJA instantaneous vorticity contours and streamlines over the actuation period with AFC off (top plots) and on (bottom plots) for gust-stalled airfoil, $\omega_a = 12.6$.

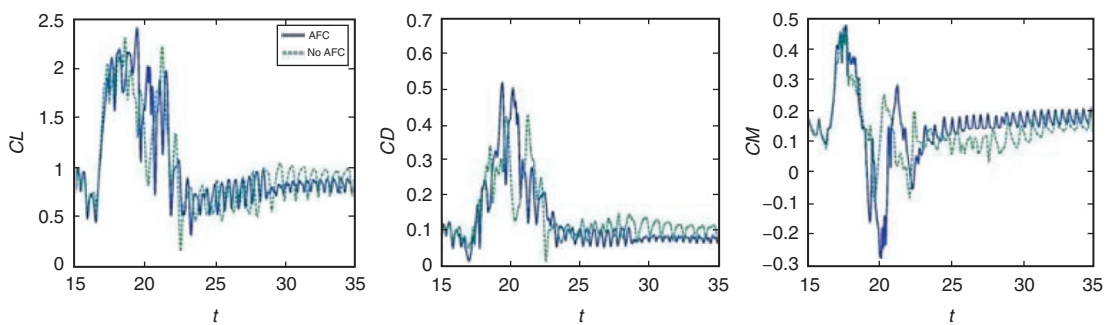


Figure 14. Airfoil aerodynamic response to SEG with AFC on and off, $\omega_a = 12.6$.

primarily shifted and in some cases even increased, hence indicating a limited AFC control authority with such actuation regime when applied to a massively separated flow. However, it is important to note that the airfoil recovery back to the steady-state oscillations following the gust passage appears to be significantly expedited by actuation.

4.4. Comparison of airfoil responses to SEG with AFC on ($\omega_a = 9$ and 12.6)

Finally, Figure 15 compares the gust aerodynamic responses with AFC on at two actuation frequencies in the case of impinging long-duration SEG with $\varepsilon_g = 0.35$ and $T_g = 10$. For $\omega_a = 12.6$, the AFC favorable effect again appears to be primarily limited to the recovery stage while it is less beneficial during the stall. On the other hand, for SJA actuation with $\omega_a = 9$ close to the shedding frequency, the impact shows a sudden dominant peak around $t = 20$ followed by a significantly subdued response afterwards. This reveals benefits of the actuation regime resonant with oscillating steady-state flow condition and thus essentially confirms $F^+ = O(1)$ optimum control criterion.

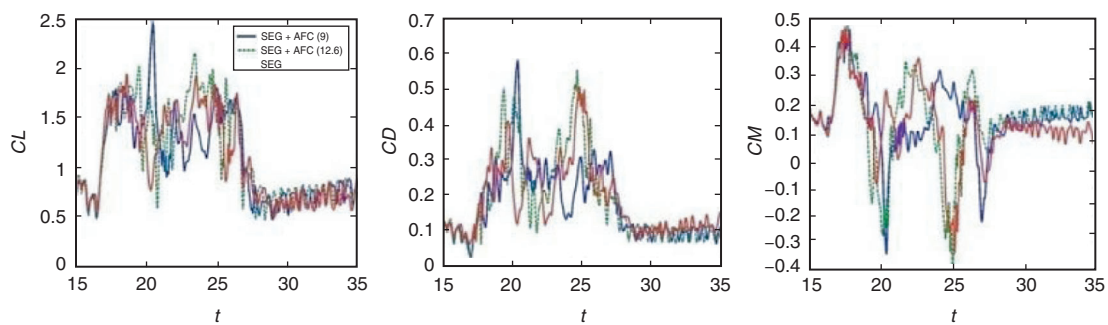


Figure 15. Airfoil aerodynamic response to SEG with AFC on and off, $\omega_a = 9$ and 12.6.

5. CONCLUSIONS

Airfoil active flow control using synthetic-jet actuation may require integration of multiple design and analysis tools to account for various geometry and unsteady flow parameters. Scaling analysis using LEM is a critical step in finding optimal SJA characteristics including actuation frequencies for the required actuator design. Further tuning requires a comprehensive CFD modeling to account for nonlinear viscous effects inherent to the internal actuator flow as well as those resulting from the jet interaction with the airfoil boundary layer.

High-accuracy numerical simulations were performed to examine effects of the SJA-based active flow control on SD7003 airfoil unsteady aerodynamic response to impinging high-amplitude sharp-edge gust. Numerical simulations were performed in the laminar flow regime with $M_\infty = 0.1$ and $Re_c = 10,000$, with the airfoil installed at the angle of attack $\alpha = 8^\circ$. In computations, the complete geometry of the actuator was *not* modeled. Instead, the actuator's orifice was embedded about $0.3c$ downstream from the leading edge in the region of a laminar separation zone observed in the steady-state flow regime. In the adopted numerical procedure, the boundary condition for time-harmonic velocity fluctuations obtained from RANS simulations of the SJA performance in a quiescent medium was imposed at the bottom of the actuator's orifice. The ratio of the orifice width to the airfoil chord was fixed at $d/c = 0.005$, and the non-dimensional actuation frequencies $\omega_a = 9$ and 12.6 were selected for the analysis.

At the steady-state flow condition, the boundary-layer tripping effect produced by the orifice cavity regularized the airfoil shedding process with notable phase and frequency shifts in the fluctuating aerodynamic response. With actuation turned on, the jet interaction with the grazing flow completely modified the axisymmetric jet structure in comparison with SJA performance in a quiescent medium. Pronounced shifts in the mean values of the airfoil drag and moment responses were observed.

With the high-amplitude sharp-edge gust impinging on the airfoil surface, the pattern of the boundary-layer vorticity dynamics dramatically changed, with the airfoil abruptly entering into the stall. In the case of actuation with $\omega_a = 12.6$, the favorable effect on the aerodynamic response was primarily limited to the recovery stage following the gust passage, while the control authority of the massively separated flow with such actuation regime was limited. In contrast, for actuation with $\omega_{SJA} = 9$ close to von Karman shedding frequency, the results revealed sudden dominant peaks followed

by significantly subdued responses afterwards, thus confirming benefit of the actuation regime resonant with the time-periodic steady-state oscillations.

ACKNOWLEDGEMENTS

The authors would like to acknowledge support for this work from the National Science Foundation, Award Number 0955970 (Program Manager Dr. H.H. Winter). The help of graduate and undergraduate students at ERAU, Ms. Nicole Fossum, Ms. Amandine Bourlier, Ms. Shibani Bhatt, Mr. Taher Surti, Mr. Mina Mankbadi, Mr. Lap Nguyen and Mr. Jacob Brodnick, participating in the project and conducting numerical analyses at its various stages, is acknowledged. Finally, the guidance obtained from Dr. Miguel Visbal (AFRL) and Dr. Scott Sherer (AFRL) in implementing high-accuracy numerical simulations is highly appreciated.

REFERENCES

- [1] Mankbadi, M.R. and Golubev, V.V., (2009), "Modeling of Acoustic Streaming for Micro Air Vehicle Propulsion and Flow Control," AIAA Paper 2009-0284.
- [2] Mankbadi, M.R., (2010), "Large-Scale Simulations of Acoustic Synthetic Jets," AIAA Paper 2010-0016.
- [3] Surti, T., Fossum, N., Mankbadi, M., Nakhla, H., and Golubev, V., (2010), "Navier-Stokes Simulations of Acoustic Streaming for Flow Control and Micropropulsion," AIAA Paper 2010-1008.
- [4] Gallas, Q., Holman, R., Nishida, T., Carroll, B., Sheplak, M., and Cattafesta, L., (2003), "Lumped Element Modeling of Piezoelectric-Driven Synthetic Jet Actuators," AIAA Journal, Vol. 41, pp. 240-247.
- [5] Smith, B. L., and Glezer, A., (1997) "Vectoring and Small-Scale Motions Effectuated in Free Shear Flows Using Synthetic Jet Actuators," AIAA Paper 97-0213.
- [6] Rizzetta, D. P., Visbal, M.R., and Stanek, M.J., (1999), "Numerical Investigation of Synthetic-Jet Flowfields." AIAA J., Vol. 37, pp. 919-927.
- [7] Mueller, T.J. and DeLaurier, J.D., (2003) "Aerodynamics of Small Vehicles," Annual Review of Fluid Mechanics, Vol. 35, pp. 89-111.
- [8] Gad-el-Hak, M., (2001) "Flow Control: The Future," J. Aircraft, Vol. 38, No. 3, 402-418.
- [9] Shyy, W., Lian, Y, Tang, J., Viieru, D., and Liu, H., (2008) "Aerodynamics of Low Reynolds Number Flyers," Cambridge University Press.
- [10] Gursul, I., Wang, Z., and Vardaki, E., (2006) "Review of Flow Control Mechanisms of Leading-Edge Vortices," AIAA Paper 2006-3508.
- [11] Williams, N.M., Wang, Z., and Gursul, I., (2008) "Active Flow Control on a Non-slender Delta Wing," AIAA Paper 2008-740.
- [12] Golubev, V.V., Dreyer, B.D., Visbal, M.R., and Golubev, N.V., (2009) "High-Accuracy Viscous Simulation of Gust Interaction with Stationary and Pitching Wing Sections," AIAA Paper 2009-0011.
- [13] Golubev, V.V., Dreyer, B.D., Hollenshade, T.M. and Visbal, M.R., (2009), "High-Accuracy Viscous Simulation of Gust-Airfoil Nonlinear Aeroelastic Interaction," AIAA Paper 2009-4200.
- [14] Golubev, V.V., Hollenshade, T.M., Nguyen, L., and Visbal, M.R., (2010), "Parametric Viscous Analysis of Gust Interaction with SD7003 Airfoil," AIAA Paper 2010-928.
- [15] Golubev, V.V., Nguyen, L., and Visbal, M.R., (2010), "High-Accuracy Low-Re Simulations of Airfoil-Gust and Airfoil-Vortex Interactions," AIAA Paper 2010-4868.
- [16] Golubev, V.V., Nguyen, L., and Visbal, M.R., (2011), "High-Fidelity Simulations of Transitional Airfoil Interacting with Upstream Vortical Structure," AIAA Paper 2011-394.
- [17] Rumsey, C.L., (2009), "Successes and Challenges for Flow Control Simulations," International Journal of Flow Control, Vol. 1, pp. 5-27.
- [18] Morgan, P.E., Rizzetta, D.P, and Visbal, M.R., (2007), "Large-Eddy Simulation of Separation Control for Flow over a Wall-Mounted Hump," AIAA Journal, Vol. 45, pp. 2643-2660.
- [19] Raju, R., Aram, E., Mittal, R., Cattafesta, L., (2009), "Simple Models of Zero-Net Mass-Flux Jets for Flow Control Simulations," International Journal of Flow Control, Vol. 1, pp. 179-197.

- [20] Visbal, M.R. and Gaitonde, D.V., (2002) "On the Use of High-Order Finite-Difference Schemes on Curvilinear and Deforming Meshes," *Journal of Computational Physics*, Vol. 181, pp. 155–185.
- [21] Suhs, N.E., Rogers, S.E., Dietz, W.E., (2002), "PEGASUS 5: An Automated Pre-processor for Overset-Grid CFD," AIAA Paper 2002–3186.
- [22] Sherer, S.E., Visbal, M.R., Galbraith, M.C., (2006), "Automated Preprocessing Tools for Use with a High-Order Overset-Grid Algorithm," AIAA Paper 2006–1147.
- [23] Seifert, A., and Pack, L., (1999), "Oscillatory Excitation of Unsteady Compressible Flows Over Airfoils at Flight Reynolds Number," AIAA Paper 99–0925.
- [24] McCormick, D., (2000), "Boundary Layer Separation Control with Directed Synthetic Jets," AIAA Paper 2000–0519.
- [25] Gillaranz, J.L., and Rediniotis, O.K., (2001), "Compact, High-Power Synthetic Jet Actuators for Flow Separation Control," AIAA Paper 2001–0737.
- [26] Holman, R., Utturkar, Y., Mittal, R., Smith, B.L., and Cattafesta, L., (2005) "Formation Criterion for Synthetic Jets," *AIAA Journal*, Vol. 43, pp. 2110–2116.
- [27] Tang, H., and Zhong, S., (2009), "Lumped Element Modeling of Synthetic Jet Actuators," *Aerospace Science and Technology*, Vol. 13, pp. 331–339.
- [28] Galbraith, M.C., and Visbal, M.R., (2010), "Implicit Large Eddy Simulation of Low-Reynolds-Number Transitional Flow Past the SD7003 Airfoil," AIAA Paper 2010–4737.